COSMIC RAY DATA IN EROSITA

Research Project Report

Presented by
Selina Nöcker
May 2, 2023

Astronomical Institute,
Dr. Karl Remeis-Sternwarte Bamberg,
Friedrich-Alexander-Universität Erlangen-Nürnberg

Supervisor: Prof. Dr. Jörn Wilms

Abstract

Analyzing the data of any detector, researchers have to be aware of background sources and how to analyze and exclude them correctly. Especially instruments which operate in outer-space, such as the eROSITA detector analyzing the X-ray structure of the whole sky, are affected by the important but unpredictable background source considered in this project: Cosmic rays. For this and many other reasons, the space weather is permanently monitored by various detectors.

This report is summarizing the work of a research project done at the Dr. Karl Remeis Sternwarte Bamberg, in which the task was to address this issue from another perspective: We wanted to find out, if it is possible to extract information on space weather from discarded background data of the eROSITA instrument that is identified and counted as minimum ionizing particles (MIPs) by an on-site rejection algorithm. If so, using this method, we could gain insight on space weather from observations by eROSITA of the X-ray sky and therefore target the background analysis for cosmic rays more efficiently. Moreover, this could improve our understanding of the cosmic environment at the Lagrange point L_2, the location of the eROSITA mission, which is a crucial site for astrophysical projects.

During the project, we developed a program to methodically extract and store the measured MIP data from the raw eROSITA measurement and housekeeping files for a given time interval and time resolution. Additionally, we compared the background data to measured sun weather data extracted in the same time range from the ACE satellite, which is dedicated to measuring space weather. In our comparison, we focused on the long- and short-term behaviour to discuss the two different types of cosmic rays contributing to the background. We found that the data extracted from eROSITA correlates well with high-energy particle fluxes measured by ACE in both time ranges. From our results concerning the short-term analysis, we could provide information about the nature of MIPs arriving at the camera. We confirmed that low-energy particles are effectively shielded by eROSITA and only high-energy particles arrive at the cameras and disturb the measurements. Moreover, we filtered the data points according to the satellite's attitude, to observe the influence of the galactic plane on the observations on eROSITA, which did not give the expected result of a significantly reduced MIP flux mean. This issue may be explored further in future investigations. Lastly, we calculated a mean velocity of particles arriving at eROSITA by cross correlating the extracted data with the high-energy component measured by ACE. Our result coincides with typical solar wind velocities.

Contents

1. Introduction: The role of X-rays and eROSITA in astrophysics

When studying the structure of our universe, the detection and analysis of X-ray radiation plays a significant role. For instance, the centers of galaxies emit a large amount of X-rays that hold information about their properties (Merloni et al., 2012). Such emitting galaxy centers are called active galactic nuclei and are one of the key elements in the process of galaxy formation and the evolution of the universe (Padovani et al., 2017). To detect the photons coming from these or other X-ray sources, such as super nova remnants, interacting stellar black holes or neutron stars, it is required to build specifically designed detectors. One requirement is their functionality in space, since our atmosphere is not transparent to X-rays. Therefore, sending X-ray-detecting satellites into orbit or even further away presents a center issue in this research.

In this project we study data from one of the latest X-ray detectors: eROSITA. eROSITA is an acronym for '**e**xtended **RO**entgen **S**urvey with an **I**maging **T**elescope **A**rray' (Predehl et al., 2021). Its center purpose is to create images of the whole sky, so-called all-sky surveys, in the X-ray waveband. To achieve this, eROSITA has a high field of view that can be used not to look at specific single sources, but at large areas of the sky simultaneously. The promise of eROSITA and its all-sky surveys is that this data is expected to constrain cosmological models helping to understand how the universe was formed and provide causes for its current state. Moreover, the data of eROSITA will help study numerous X-ray sources and shed light on the physics of their structure and evolution.

However, the functioning of an outer-space detector is challenging due to the significant influence of charged particles from the universe on the signal background (Freyberg et al., 2020). In some worst-case scenarios, observations are hardly possible or the measured data is unreadable at increased cosmic ray activity (Kirsch, 2018). Originating e.g., in the sun, such particles can damage or destroy its parts upon impact. This is one of the reasons for the limited lifetime of outer-space detectors. Moreover, such foreign particles can interact with the detector and tamper with the measured readout of the observed target. Therefore, studying the current situation of cosmic rays during an astrophysical experiment such as an X-ray observation is essential for the data analysis and interpretation afterwards.

The report is structured as follows: Following the general introduction, we briefly introduce the basic theory of cosmic rays and the influence on outer-space detectors in Section 1.1. Next, Chapter 2 gives a brief overview of the primarily discussed detector, eROSITA, and its properties. We will describe some commonly occurring background signals and go into more detail on the affect of high-energy particles on the detector readout and the method to account for cosmic rays developed for eROSITA. The small Section 2.2, is attached to give insight on the sun-monitoring detector ACE, whose data we used for comparison in this project. In Chapter 3, we elaborate on the extraction method of the desired measurement data from eROSITA and briefly document the equivalent process for ACE. After that, we present our results of the comparison of measured cosmic rays in eROSITA and ACE in Chapter 4. Here, we start by providing a general overview of the data in Section 4.1, followed by a demonstration of the filter used for smoothing the data in Section 4.2. Then, we provide our results concerning both long-term (Section 4.3) and short-term

analysis (Sections 4.4 and 4.5) of the data. We continue by analyzing the influence of the angular orientation on the measurement of cosmic rays in Section 4.6 and end the chapter with the insights we gained by applying a cross correlation on the data sets in Section 4.7. Lastly, we conclude this report in Chapter 5 with a summary of our results and propose ideas to further investigate the impact of cosmic rays on eROSITA and other outer-space detectors. Appendix A contains a selected data extraction code.

1.1. Cosmic rays

Since any detector observing in outer-space, including eROSITA, is exposed to cosmic rays, they strongly influence the detector and its readout. For this reason, the importance of understanding the nature of cosmic rays is undisputed. Therefore, we will summarize the fundamental theory concerning cosmic rays in the following section.
Cosmic rays are highly energetic particles, the major component being protons (Blasi, 2013) that originate either in the sun or arrive from outside of the solar system. They are then labeled solar and galactic cosmic rays, respectively. First detected by balloon flight measurements in the early 1900s (Hess, 1912), cosmic rays largely contribute to the space weather in our solar system. To give a brief insight, we will discuss the two different cosmic ray components and how they can affect an X-ray detector on the example of eROSITA.

1.1.1. Solar and galactic cosmic rays

Galactic cosmic rays are, as mentioned above, defined by their origin, i.e., they are created outside the solar system, for example in supernova remnants (Blasi, 2013) or active galactic nuclei (Anchordoqui, 2019). Their flux remains approximately constant and is only slowly varying with time.
Solar cosmic rays can be separated into two groups according to their emission timescale. Discrete ejections from the sun within shorter periods create a sudden flux of solar energetic particles (SEPs). These bursts are induced by releases of energy from the magnetic field of the sun and originate either from solar flares happening over several hours or coronal mass ejections (CMEs) lasting days (Reames, 1999; Schwenn, 2006).
The long-term emission in the span of multiple years, the so-called solar wind, presents itself as a continuous flow of thin magnetised plasma, a mixture of electrons and ions, and is again divided in a slow and a fast component (Schwenn, 2006). By moving charged particles, the solar wind generates a magnetic field affecting the whole solar system. This consequently evokes an interaction with the planetary fields, resulting e.g., in extended magnetotails.
The intensity relation between solar and galactic cosmic rays varies periodically, which is caused by the activity cycle of the sun. With a total period of around eleven years, the flux intensity of the solar wind and the recurrence of particle bursts rises and falls in a sinusoidal way (Hathaway, 2015), as is shown in Fig. 1. The relation between solar and galactic cosmic rays follows this cycle due to the varying amount of solar cosmic rays and the shielding and deflection power of the solar wind affecting the arrival of galactic cosmic rays. The measured data analyzed in this project covers the years 2019–2022 (Predehl et al., 2021), where solar activity was beginning to rise again after a minimum at the end of 2019 (Geryl and Alvestad, 2020). Due to that, the sample size of flares or bursts in this project is expected to be small and only starting to rise. On the other hand, the galactic cosmic ray flux was at its maximum around the launch date and is beginning its decrease after the solar activity minimum, which should present itself in the quiescent cosmic ray background of the detector. This is in agreement with the analyzed data, as seen later in Chapter 4.

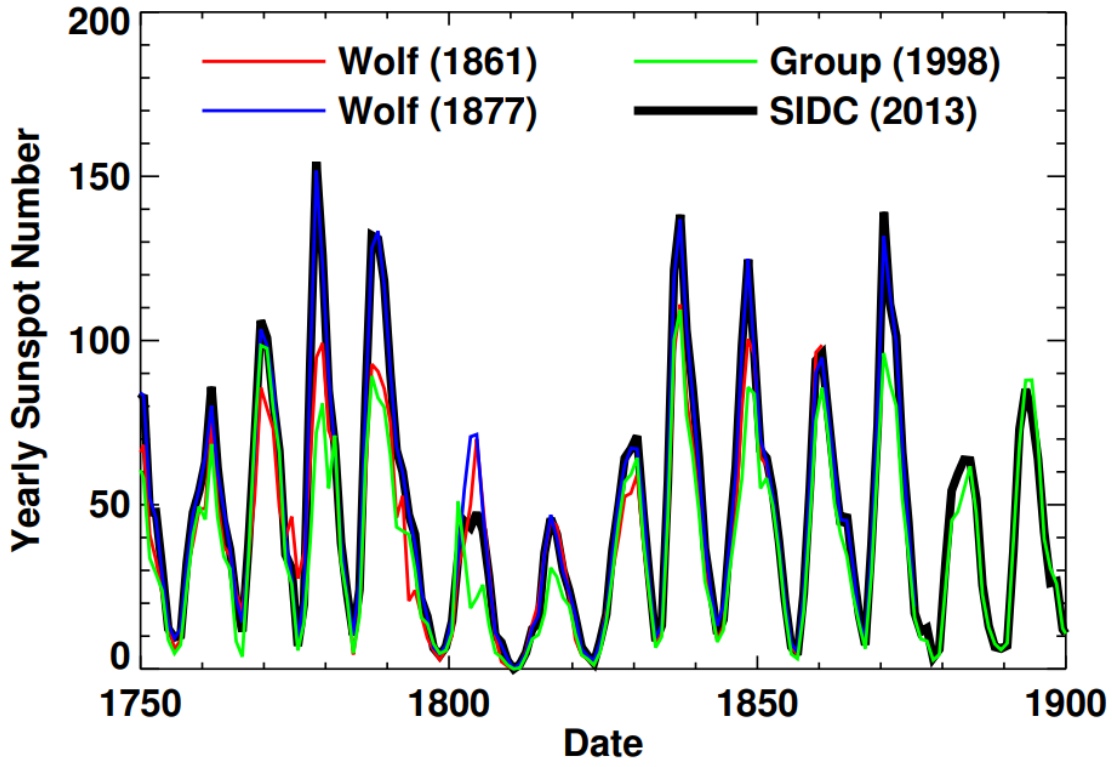

Figure 1: Solar cycle represented by the yearly sunspot numbers as reported by Wolf, 1861 (red line), Wolf, 1877 (blue), Hoyt and Schatten, 1998 (green), and by SILSO, 2014 (black). Although this shows a visible variation in amplitude and disagreement between different sources, the sinusoidal flux variation is undeniably visible. (Figure taken from Hathaway, 2015.)

2. The detectors in the project

In this chapter, we will introduce the detectors that measured the provided data for this project. First, we will give insight on the technical composition, common background sources and the initial observations of eROSITA. We will especially set our focus on the influence of high energy particles on the data readout of eROSITA and the developed method to eliminate such compromised data. The information presented in this chapter is primarily based on References Predehl et al., 2021 and Freyberg et al., 2020. After that, we will briefly present ACE.

2.1. eROSITA

eROSITA is a German X-ray detector mounted on the Russian spacecraft 'Spectrum Roentgen Gamma' (SRG) (Pavlinsky et al., 2018) and a product of scientific cooperation between the European and Russian space agencies. SRG was launched into space on the 13th of July in 2019 from the Baikonur cosmodrome in Kazakhstan. It operates in a halo orbit around the second Lagrangian point L_2, which is $1.5 \cdot 10^6$ km away from the earth in the sun-earth direction, see Fig. 2 for representative illustrations.

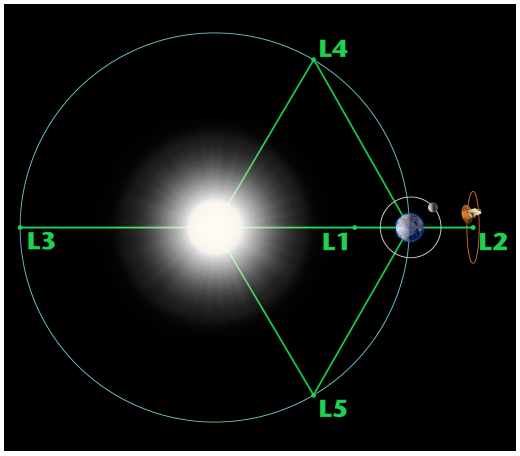

(a) Map of the Lagrangian points in the sun-earth system, not to scale. The orange object represents a detector orbiting around the L_2 Lagrangian point. (Figure taken from NASA/WMAP Science Team, 2018)

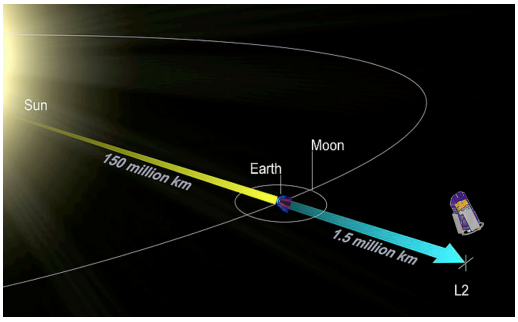

(b) Illustration of the L_2 orbit of the eROSITA detector on the SRG spacecraft. eROSITA will be the first X-ray telescope located at L_2. (Taken from Merloni et al., 2012, Fig. 3.1.1)

Figure 2: Two schematic images on the location of the L_2 Lagrange point.

The main goal of eROSITA is to perform eight all-sky-surveys, meaning that the detector will scan and measure the whole sky for X-ray radiation to form a map that shows all detected sources. There are eight surveys planned, each taking half a year to measure. This results in four years of observation time in total for all surveys. Not included are calibration measurements or pointed observations. With these maps, it is predicted to discover many new astronomical X-ray sources. Its predecessor, ROSAT (acronym for **RO**entgen **SAT**ellite), catalogued around 125 000 new sources (Voges et al., 1999). ROSAT operated from 1990 to 1999 and was the first detector to perform such a survey in the X-ray waveband (Truemper, 1982). With the development in technology, the increased sensitivity and resolution of eROSITA are expected to lead to a significantly increased number of newly detected sources. Therefore, eROSITA is expected to catalog millions of objects, including at least 100 000 clusters of galaxies (which are gravitationally bound assemblies of many galaxies), a few million active galactic nuclei and around 700 000 active stars (e.g. Pillepich, Porciani, and Reiprich, 2012; Merloni et al., 2012). The first survey that was completed and published in a press release in June 2020 (Max Planck Institute for extraterrestrial Physics, 2020), see Fig. 3, already detected 1 004 624 new X-ray sources (Predehl et al., 2021).

2.1.1. Structure of eROSITA

In this section, we give an outline of the structure of the eROSITA detector and explain the basics of its most important parts. The total weight of eROSITA amounts to approximately 800 kg, including its electronics, a heating system to keep the components at operating temperature, the surrounding shielding, and lastly eROSITA's main feature: the seven specifically designed mirror assemblies. The structure is shown schematically in Fig. 4.
Every assembly consists of 54 Wolter-shaped mirrors (Friedrich et al., 2008), a filter wheel and

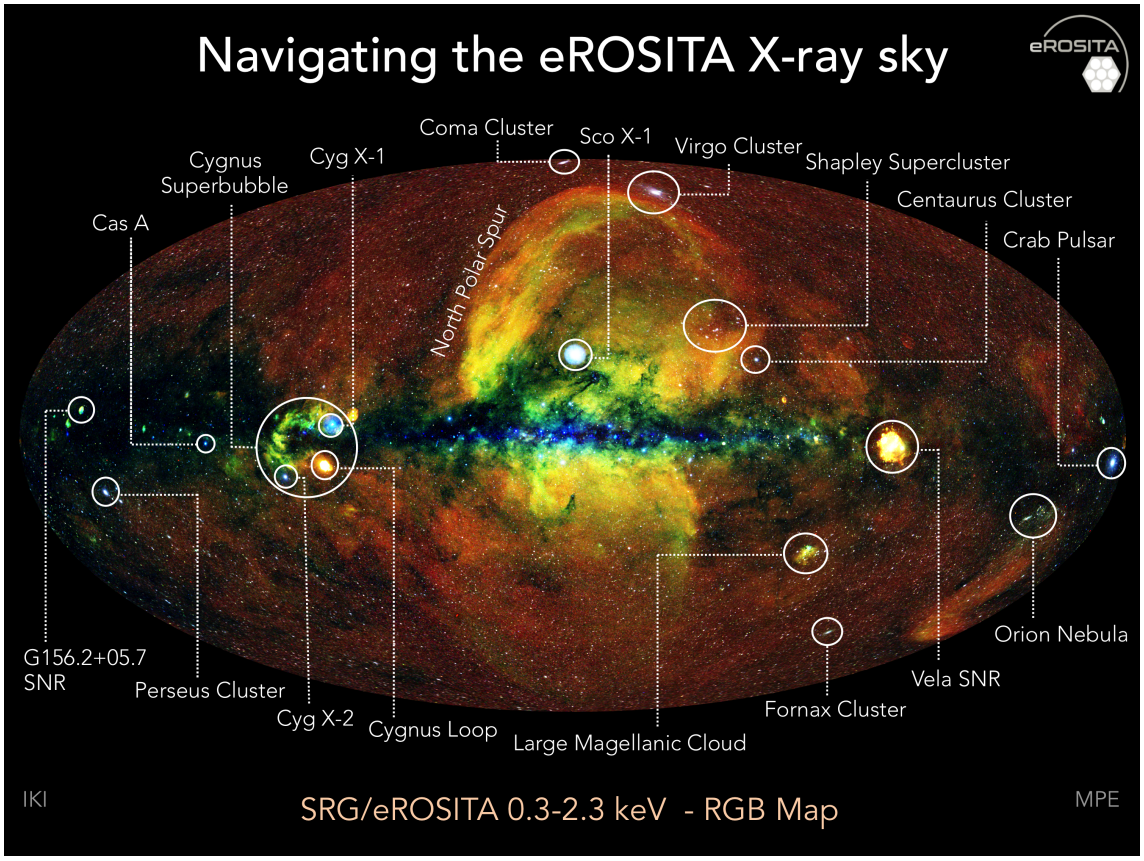

Figure 3: The first survey of the eROSITA detector in a galactic coordinate system with annotations of well-known X-ray sources. (Figure downloaded from Max Planck Institute for extraterrestrial Physics, 2020)

a CCD-camera (abbreviated for Charged-Coupled Device) (Meidinger et al., 2014). The Wolter mirrors, which are specifically shaped mirrors to efficiently focus X-rays, are stacked concentrically with increasing radius. The second component, the filter wheel, enables the operating researcher to control the allowed incoming light arriving on the camera. The filter wheel has the self-explanatory options ‘OPEN’, ‘FILTER’, ‘CLOSED’ and ‘CALIB’, with ‘FILTER’ being the standard setting for observations. The detecting camera itself, the CCD, detects the photons by their separating of ionized charges in the pixel material and sends a corresponding voltage to the electronic system.

2.1.2. Common background components of eROSITA

As mentioned before, many background signals that do not hold information about any sources in the sky contribute to the detector readout. Therefore, the camera output has to be carefully analyzed to accurately depict the X-ray energy distribution of the sky. Before such images can be extracted from the raw data, these background sources have to be recognized and removed. Simulation studies for the high energy particle background arising in eROSITA measurements were already conducted years before the detectors launch in 2019 (Tenzer et al., 2010; Perinati et al., 2012). Background signals can arise from various origins, including the sky and the detector itself (Freyberg et al.,

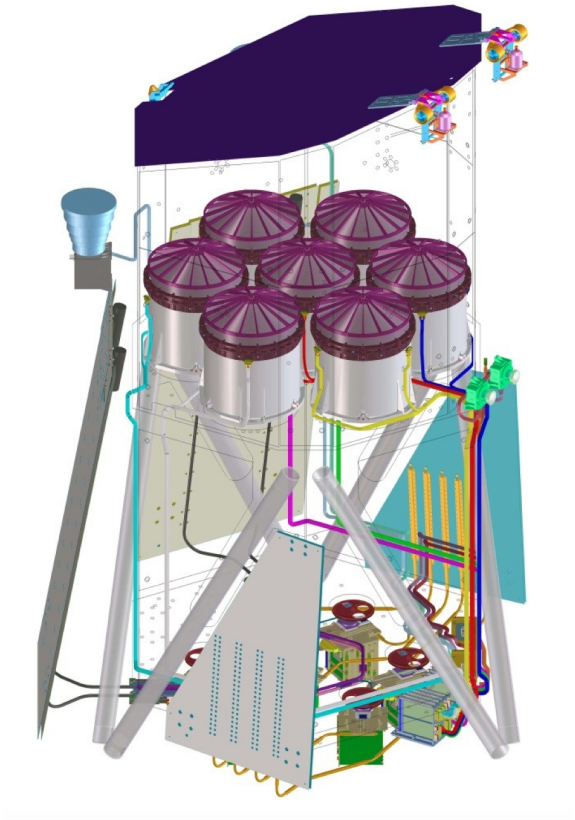

Figure 4: A sketch of the structure of eROSITA. (Taken from Predehl et al., 2021, Fig. 1)

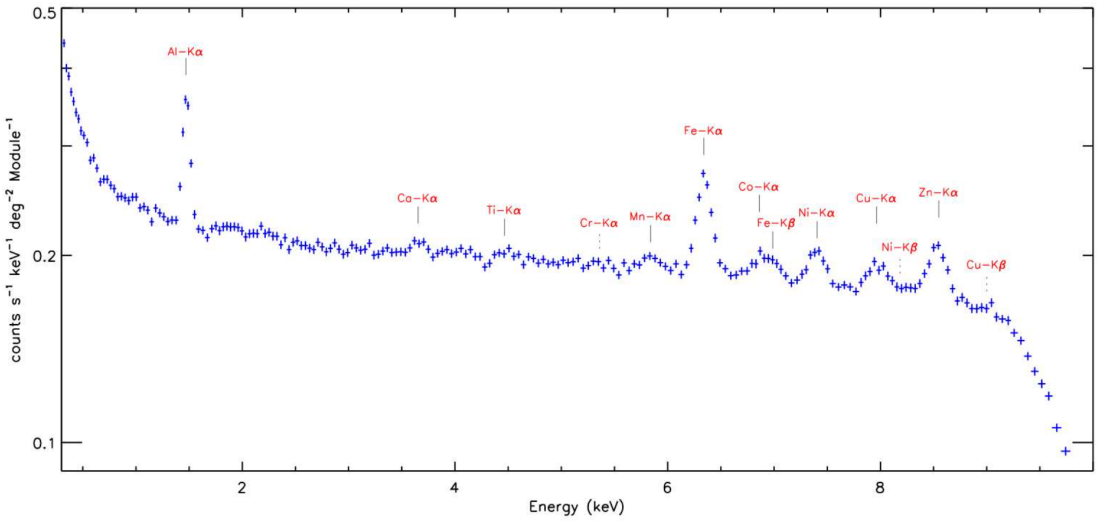

Figure 5: Average spectrum of a measurement with the closed filter setting to depict the background arising due to the shielding material. (Taken from Freyberg et al., 2020, Fig. 4)

2020). In the following, we will describe three examples of common background components that eROSITA detects unintentionally: The contribution of the shielding material, the influence of optical light and the detection of cosmic rays.

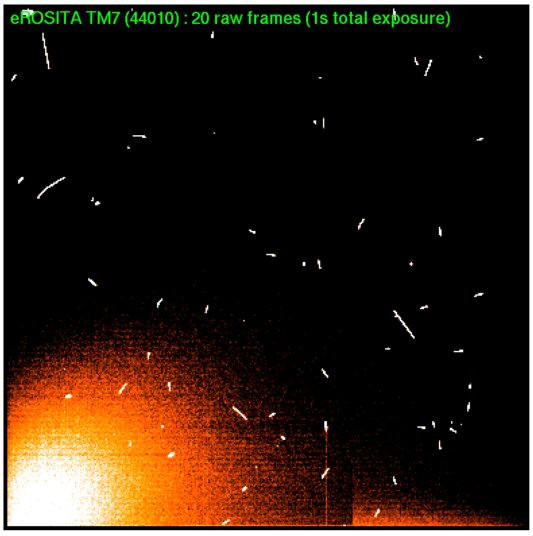

(a) Camera image of an optical light leak. On the lower left one can make out an accumulation of detected photons. Here, light can slip through a gap below the filter and arrive unimpeded at the CCD camera.

(b) Camera images with cosmic rays. In all four frames, ray-shaped structures with high intensity are scattered over the image.

Figure 6: Camera images of eROSITA showing different background influences. (Figures taken from Freyberg et al., 2020, Fig. 7)

The first aspect can be seen in Fig. 5, where the spectrum of a camera captured with the closed filter window is shown. Hence, we see the energy distribution of detected photons without any incoming light from the sky. The spectrum shows a declining slope that includes some distinct peaks at fixed energies. The declining shape can be derived from the camera sensitivity, whereas the peaks arise through known resonances of the shielding material, e.g., emission lines from aluminium (Al) and iron (Fe).

Secondly, visible light from luminous optical sources can contribute to the detected signal. In front of all cameras, thin aluminium layers are installed to act as a mirror for incoming optical photons. However, to avoid accidentally absorbing signal-relevant X-rays, this layer has to be comparatively thin (approximately 200 nm, corresponding to a suppression factor of 10^{-5}–10^{-6}) and is therefore not able to effectively deflect concentrated optical light from luminous sources, for instance bright stars or Jupiter. Since eROSITA is completely rotating every 4 h to observe the whole sky, this contribution of sunlight is measured in a periodic fashion, which consequently is seen in the analyzed data, see, e.g., Section 4.4. In the case of cameras 1, 2, 3, 4, and 6, this layer is deposited onto the CCD camera itself, whereas cameras 5 and 7 have the layer only on the filter wheel with the ‘FILTER’ setting. Therefore, if optical light arrives from a certain angle for cameras 5 and 7, it can slip through a small open gap without obstruction between camera and filter. This gives rise to the so-called ‘optical light leak’ effect, which is depicted in Fig. 6a for camera 7. There, an accumulating intensity is shown in the lower left, corresponding to this optical leak.

2.1.3. Cosmic ray background in eROSITA

In the following section, we will focus with more detail on the influence of the background source mentioned last, cosmic rays, on the eROSITA detectors. As explained in the preceding Section 1.1, cosmic rays are highly energetic particles originating either in the sun or outside of the solar system. Outside the Earth's atmosphere and magnetic field, the detector is not protected against these particles. On average, one to three cosmic ray particles reach a camera per readout cycle on eROSITA (Predehl et al., 2021). They damage the functionality of the detector components and influence the measured signal (Freyberg et al., 2020). The shielding of eROSITA reduces the arriving amount of high energy particles, but cannot protect it completely. If a cosmic ray enters the detector, it deposits energy in the parts where it can pass through. The mean energy loss per particle is commonly referred to as a mass stopping power, which can be accurately described for the regarded energy range via the so-called Bethe equation (Tanabashi et al., 2018). The rate of the mean ionizing energy loss radically decreases with momentum at first, which is followed by a turning point, a minimum, and after that, it increases logarithmically. Particles that carry a momentum resulting in a mean energy loss matching that turning point are called minimum ionizing particles (MIPs). MIPs are the most common particles to pass through the shielding of an outer-space detector (Kirsch, 2018).
Such particles can become particularly dangerous for the detector when they hit crucial electronics in the system and cause various errors (Adams, 1985). Moreover, the rate of incoming MIPs is strongly connected to the lifetime of a detector, as the solar panels that power the detector gradually degrade and loose their efficiency due to their interaction with high energy particles (Horne et al., 2013; Crowley et al., 2016). For the analysis in Chapter 3, especially the details of the influence on the CCD readout become important: If cosmic rays hit the camera, they deposit their energy throughout the pixels, most likely in a ray-shaped structure. Because of the high energy release, the affected observation frame gets corrupted and the pixels that detected the particle have to be ignored for further analysis. Four selected camera frames showing detected MIPs that present themselves as ray-shaped high intensity structures are seen in Fig. 6b.
Since the pixel information on these MIPs takes up an immense amount of data space and gives no information on the sought-after energy distribution of the sky, these rays are recognized and removed by the detector on-site with a rejection algorithm, specifically developed for eROSITA (Freyberg et al., 2020). This results in an increase in data capacity of the detector and therefore prolongs the duration between downloading times. More importantly, this significantly lowers the energy cost in the telemetry processes, which send the measured data to the receivers on earth.
In the following, this elimination program applied on eROSITA is explained. A cosmic ray deposits an energy in the pixels which is unusually high compared to that of a measured X-ray in the detector. Since the readout rate of 50 ms can be assumed to be fast enough, the probability of two X-rays hitting the same pixel in a single frame is generally very low. Therefore, with a defined threshold energy $E_{\text{threshold}} \approx 9\text{–}10\,\text{keV}$, the detector marks every pixel that reports a higher energy than this limit. They are then labeled trigger pixels. Since the high energy detected from MIP at the trigger pixel can cause the neighboring pixels to also be affected, they are excluded as well out of

precaution. In eROSITA, the default "rejection radius" around a trigger pixel is two pixels, meaning that the area going two pixels up, down, to the right and to the left from the trigger pixel is rejected. This results in an additional 24 pixels surrounding the one trigger pixel that are eliminated from the readout data. Interestingly, because cosmic rays trigger many pixels in a ray-shaped structure, the rate of rejected pixels to triggered pixels is not 24:1, which would be the case for isolated triggered pixels, but rather in the range of 8:1.
This algorithm efficiently filters MIP data from the measured frames on the spacecraft, however, follow-up investigation on ground is necessary. Due to imperfections of the algorithm, not 100 % of the cosmic rays are recognized and there is still affected data that remains undetected. This residual cosmic ray data in the measurement files can also be seen later in the results in Chapter 4. Secondly, for luminous X-ray sources the event of two X-rays simultaneously hitting one pixel in one frame can become non-negligible. Therefore, the eliminated information for the centers of these sources cannot be restored. However, this can be salvaged in hindsight by reconstructing the anticipated point spread distribution function of a point source with the remaining data of the edges of the source.

2.2. ACE

In our analysis, we want to compare the data of the eROSITA detector with a solar particle monitor which intentionally measures the solar wind to interpret the measured MIP flux and its accuracy. The '**A**dvanced **C**omposition **E**xplorer' ACE, orbiting the Lagrangian point L_1, is a mission from NASA to investigate energetic particles ejected by the sun or of galactic nature (Stone et al., 1998a). The applied data is provided by the Solar Isotope Spectrometer (SIS) instrument on ACE, which is aimed to study solar particle events, anomalous cosmic rays and low-energy galactic cosmic rays (Stone et al., 1998b). The device is composed of two groups of silicon (Si) detectors, which are stacked on top of each other. The SIS is able to retrace particle trajectories and can resolve energies from $\approx$ 10–100 MeV nucl^{-1}. The data shows the real-time integral flux of high-energy solar protons, averaged over five minute intervals, and distinguishes between particles with kinetic energies above 10 MeV and above 30 MeV. The proton flux p has the unit cs$^{-2} \cdot$ sec$^{-1} \cdot$ ster^{-1}.

3. Extraction and preprocessing

In the following two chapters, we will present the research carried out in this project. We will begin in this chapter by showing how we extracted and treated the raw data of both detectors. In Chapter 4, the scientific results are presented.
Since a main part of this work was the construction of the model for the extraction of MIP events from the raw eROSITA data, we initially guide through its main points. We will explain how the desired information is stored in the raw files of eROSITA and give a rundown of the extraction program developed throughout the project. In the end of the chapter, we mention the extraction of the proton flux data from the ACE instrument. An example of the MIP extraction code is given in Appendix A.1.

3.1. The extraction program for eROSITA

The raw data of the eROSITA measurements is archived on the server of the Dr. Karl Remeis-Sternwarte Bamberg and accessible for all researchers at the observatory. The data is arranged by "eROdays", the date system used for the detector, and saved in the FITS format. One eROday corresponds to one rotation of the detector around itself, resulting in a 4 h time duration. The eROday number 1 started on January 1, 2000 00:00 in Moscow time (Freyberg et al., 2020). All data concerning the measurements is saved in 'Event' files, whereas all technical data around the detection process, e.g., the status of certain valves, information on the electronics or voltages, is saved in 'Housekeeping' files. Moreover, eROSITA keeps 'Attitude' files to match the coordinates and 'Map' files for calibration information.
To read out the counted MIP events, the files starting with `H_SciHKA` need to be accessed. There, both the number of trigger pixels as well as the amount of rejected pixels per readout cycle are counted in the 'MIP-Pixel' and 'SUM' columns. If the number of MIP events exceeds a certain limit, the information is stored separately in the `H_SciHKA8` and `H_SciHKA9` files. In the former, the trigger pixels are counted in the 'MIP-pixel' column, whereas in the latter, the number of rejected pixels is documented in the 'SUM' column. Since we are interested in the amount of trigger pixels, we systematically extract the columns 'MIP-pixel' from `H_SciHKA8` and 'MIP-Pixel' from `H_SciHKAA`, depending on the amount of MIP events. There are more columns storing information about events that are discarded for the X-ray analysis, namely the column 'discardedFrame' in the files starting with `H_SciHKA01`, the counts of 'discardedMPEvents' in `H_SciHKA10` files, a column counting the 'discardedPixel' in files beginning with `H_SciHKA9` and information about 'Discarded Illegal Pattern' in `H_SciHKAC` files. After extracting the data of this additional columns in the same manner as before with a time resolution of $1\,\text{eROday} = 4\,\text{hrs}$, it becomes clear that most of the MIP information is stored in the MIP-Pixel and SUM files. As shown in an overall comparison of all available MIP counters in Fig. 7, the contribution of discarded Events from the other named columns is negligible.
When extracting the number of events in the MIP-Pixel columns, one has to be aware of the counting mechanism in the detector: The columns count in each readout cycle the number of pixels that are dismissed from the event file and add this number to the prior entry of the previous cycle. This

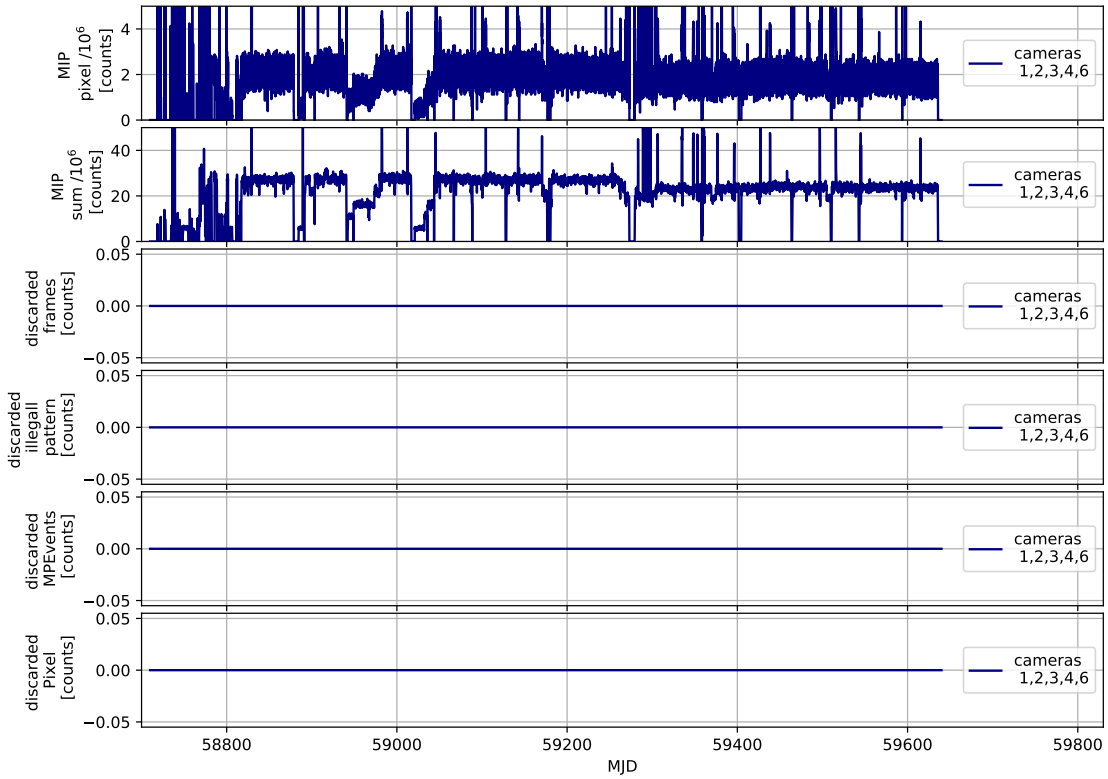

Figure 7: Overview of all collected data from the available MIP counters.

accumulates to an upper limit of $2^{16} = 65536$, where it restarts again at zero (Freyberg et al., 2020). In the program extracting the MIP data this is considered by using a loop that adds $2^{16} - 1 = 65535$, whenever the running entry is smaller than the preceding one in the MIP counter. The last entry of the counter which is below the limit is added at the end of the loop to complete the pixel count.
Since the extraction mechanism does not identify every MIP arriving at the detector without fail, we decided to additionally compare our extracted data with the information stored in the actual measurement output of the eROSITA X-ray detector. Therefore, we also extracted the data length of the 'Event files', since one entry corresponds to one measured event. With this, we can compare the MIP-counter with a counter of the events recognized as an X-ray.
Initially, the program extracted one MIP value for one eROSITA day, counting over one whole file. However, because a resolution of four hours is comparably large when studying specific sun ejection events, we wrote programs to extract extended files for the counters averaged according to a user-selectable time resolution. In this work, we used e.g., 1200 sec (20 min) and 12 sec. Additionally, in the final program one can limit the time period to certain begin and end dates, for instance around a solar eruption, to reduce the overall duration that is needed to extract the data from the raw files.
Moreover, because the algorithm of eROSITA merely counts the rejected pixels, we recalculate our data to a flux with the given effective area and readout time (Kirsch, 2018). This can be obtained in detail by taking the differential flux for particle monitors by the example of (Sullivan, 1971), however that was not relevant within the framework of this project. Because the extracted data are

counts, we can determine this via a simplified definition for the flux F, using the exposed CCD area A_{exp} and the exposure time T_{exp}:

$$F = \frac{\text{counts}}{A_{\text{exp}} \cdot T_{\text{exp}}}. \tag{1}$$

For eROSITA, the image area is $A_{\text{exp}} = 28.8\,\text{mm} \times 28.8\,\text{mm}$ (Meidinger et al., 2014) and the exposure time corresponds to the chosen time resolution as explained above, for instance 1200 sec. Furthermore, some data points that deviate largely from the measurement flux, therefore having a high difference from neighboring data, are excluded by considering the slope between two consecutive points. For the event and data files, we set a limit above which a point is labeled invalid. In the following, we will refer to this as a 'slope selection'. The limit was set to 10^6 and 10^3, for the event and MIP files respectively.

3.2. ACE

As mentioned before, we need some data that accurately depicts the cosmic wind, to be able to compare our extracted MIP data from the eROSITA files to the measured particle activity in the solar system. In the interest of this comparison, data from the SIS detector on the ACE satellite was extracted online on May 24., 2022 by C. Kirsch from the online archive of the National Oceanic and Atmospheric Administration (NOAA)[1] (Zwickl et al., 1998).
All online data was combined to one FITS file 'combined_data.fits' to facilitate easy access in the analysis process. Data points that were labeled as 'missing data values' by setting them to 10^{-5} (see header of the original online files) were excluded in our modified data set for ACE. Whenever this value was registered, the five minute average did not contain an event or the measurement process had an error. Furthermore, single data points far from the measurement line, usually unexpectedly high points above 10^3, were ignored as well. This was again done using an extraction barrier in the discrete slopes between two data points, as explained above for eROSITA data.

[1] accessible via https://sohoftp.nascom.nasa.gov/sdb/goes/ace/daily/

4. Results

Using the extracted and modified data, we continue our report by comparing the eROSITA MIP counter flux and the ACE proton flux in various ways. We start with explaining the methods that were applied to improve the legibility of the data, including making use of the Savitzky-Golay filtering method. Then, we compare the long-term as well as the short-term behaviour. After that, we will discuss, how the Milky Way has influenced the measurement of high energy particles in the eROSITA cameras. Lastly, we will cross correlate the MIP counter flux measured by eROSITA with the high-energy component measured by the ACE SIS detector to calculate a reliable value for the time lag between the two instruments.

4.1. General comparison

To get an overview of our extracted data, we begin by comparing the whole data sets of both observatories. In the beginning, we considered the camera counts of the eROSITA data separately, as shown in the top of Fig. 8. After considering this figure, we decided to accumulate the camera contributions into one quantity to achieve a more ordered picture. Moreover, because of summing over the camera MIP counters, flare events are expected to show more significant count increases. However, we left out the information supplied by cameras 5 and 7 due to their previously explained filter setting, see Section 2.1.2. The resulting overview can be viewed in the bottom image of Fig. 8. Lastly, to get to the presented plot in Fig. 9, we applied the slope selection as explained in Section 3.1, to rid the figure of strongly diverging data points.

4.2. Savitzky-Golay filtering

Because the MIP data of eROSITA shown in our comparison figure, Fig. 9, is still relatively noisy, we looked at possible smoothing variations by applying a Savitzky-Golay filter with different window sizes and orders onto the data set. For this, we used the function `savgol_filter`, available in the python package `scipy.signal`. Four possible variations are shown in the top figure in Fig. 10, with the original data on the top. We observe an increase in smoothing of the data when going downwards in the figure. To visualize the Savitzky-Golay filtering in another approach, the bottom figure in Fig. 10 shows the filtered signal lain on top of the raw data.

4.3. Contribution of galactic cosmic rays

In order to look at the two different cosmic ray components, we need to visualize the data differently. The galactic cosmic rays are featured as a continuum level, whereas the solar cosmic rays correspond to elevated flux in short timescales. Therefore, for the solar component, we will constrain our time range to previously determined intervals, where solar short-term bursts appear. For this, we refer to the following two sections, Section 4.4 and Section 4.5. However, to consider the galactic cosmic ray contribution, we have to investigate the long-term behaviour in both ACE and eROSITA data. We start our analysis with the beginning date of the all-sky-surveys, December 13, 2019, which corresponds to MJD 58830 (Predehl et al., 2021). This date exactly matches the minimum of the

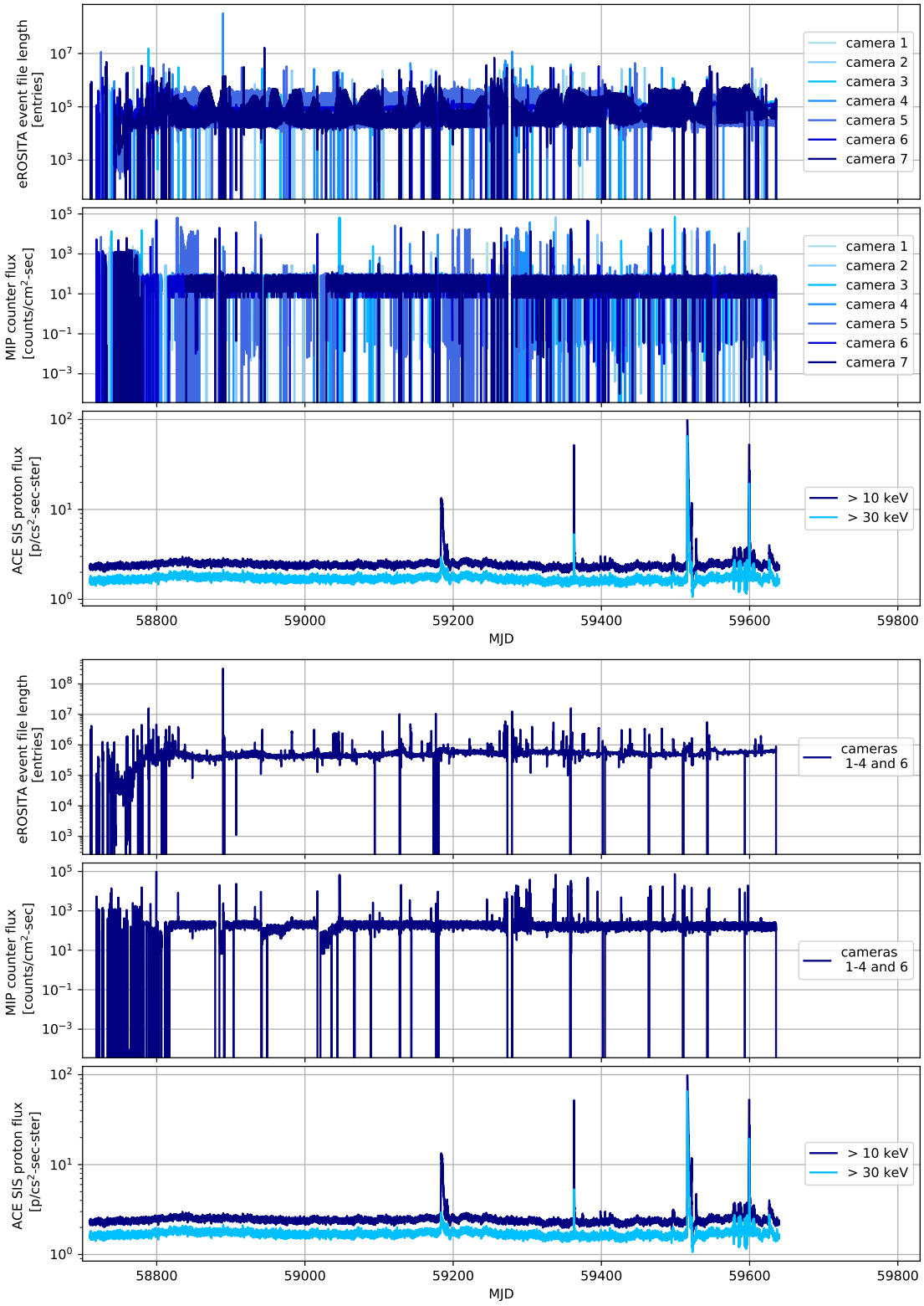

Figure 8: Overall comparison of the whole extracted time interval without slope selection. In both figures, we show from top to bottom the event file length of eROSITA, the MIP counter flux in the eROSITA files and the ACE SIS proton flux data. Top: Comparison with eROSITA data divided by the separate cameras. Bottom: Comparison with the summed up contribution of the cameras.

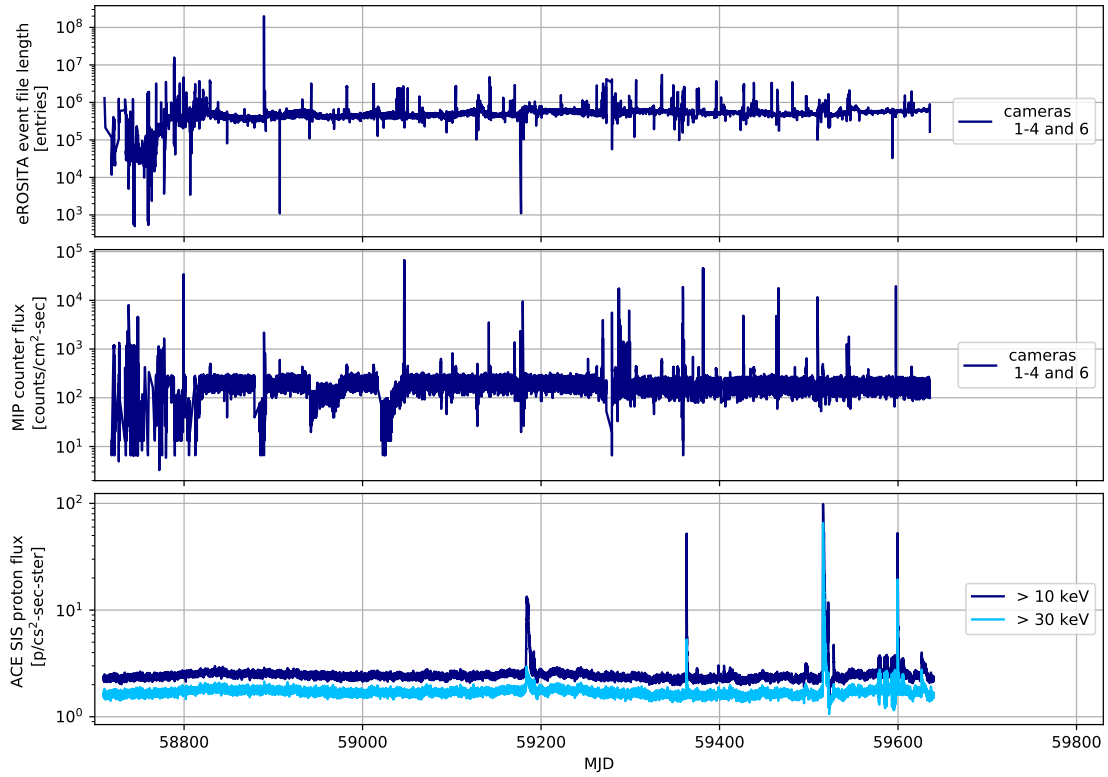

Figure 9: Overall comparison of the whole extracted time interval after the slope selection as described in Section 3.1.

solar cycle number 25, which was in December 2019 (Geryl and Alvestad, 2020). The solar cycle minimum is shown in Figure 11 with light blue background coloring.

As explained in Section 1.1, the flux of galactic cosmic rays is inversely related to the 11-year solar cycle. Therefore, we would expect to find a maximum contribution of galactic cosmic rays in the long-term contribution to the data with an overall subsequent decrease. Over the observed period of 805 days, which corresponds to approximately 2.2 years, the MIP flux decreases from a mean, averaged over 20 data points, of $219\,\text{counts} \cdot \text{cm}^{-2} \cdot \text{sec}^{-1}$ to a mean of $183\,\text{counts} \cdot \text{cm}^{-2} \cdot \text{sec}^{-1}$, whereas the ACE flux data begins at a mean of $1.81\,\text{cs}^{-2} \cdot \text{sec}^{-1} \cdot \text{ster}^{-1}$, and ends with a mean of $1.58\,\text{cs}^{-2} \cdot \text{sec}^{-1} \cdot \text{ster}^{-1}$. Consequently, this decrease is recognizable to some extent in both MIP and proton flux data sets. To get more definite results, we would suggest a follow-up investigation using a longer time period.

Moreover, in the ACE data in Figure 11, we can observe the so-called time lag between solar activity and galactic cosmic rays, which was already studied before (Tomassetti et al., 2017; Iskra et al., 2019). Between solar activity and the response in the galactic cosmic ray flux, a modulation of the ace proton flux with a time lag of around 8 months can be observed in the long-term evolution (Tomassetti et al., 2017). This results e.g., in the development of a plateau at the end of the minimum of the solar cycle, as also discussed by Freyberg et al., 2020.

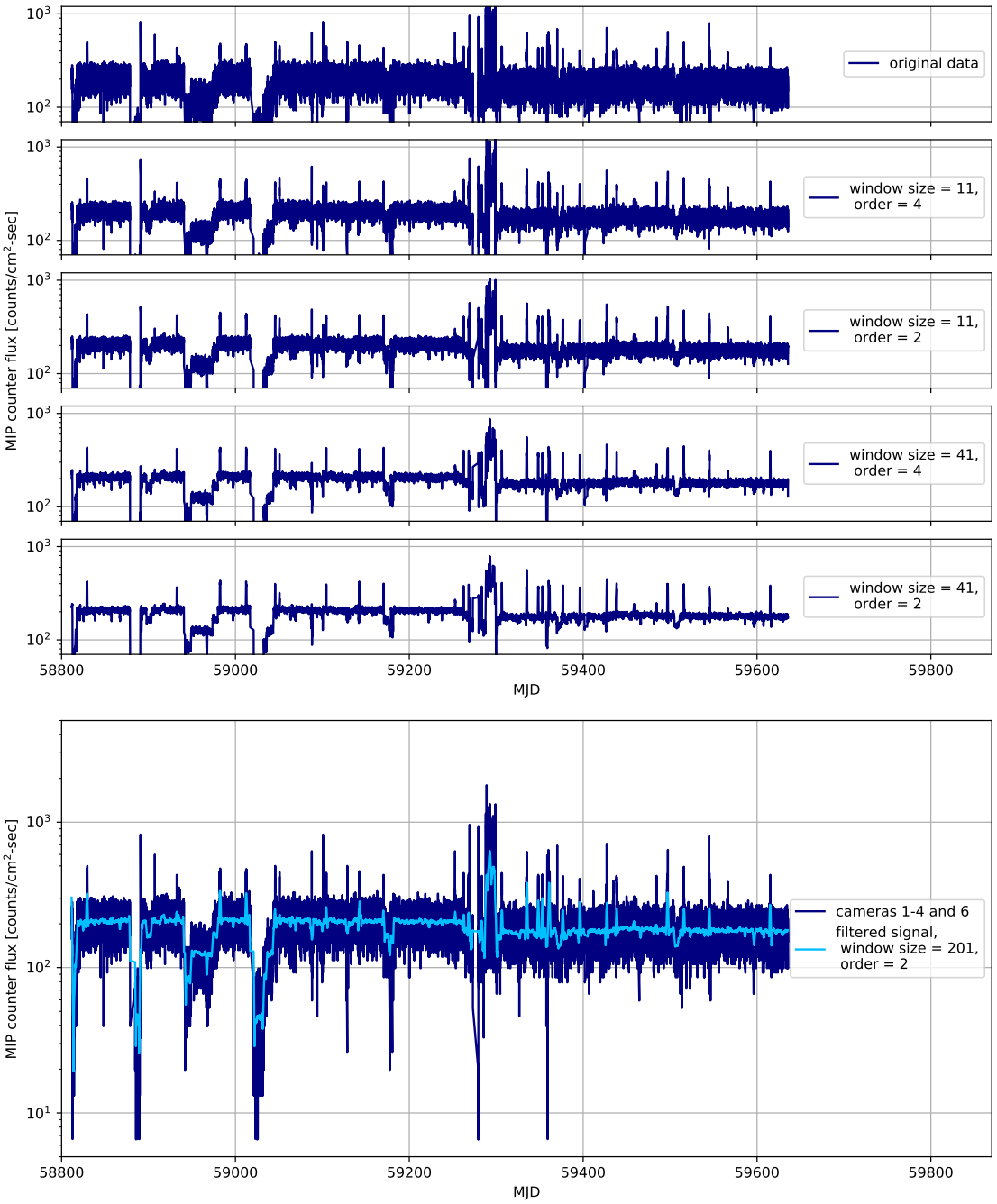

Figure 10: Two alternative illustrations of the smoothing effect by applying Savitzky-Golay filters. The top plot shows the variation of the filter for different parameters. There, the most upper plot shows the unfiltered MIP flux data for comparison. The combinations of the input variables window size and order are from top to bottom: (11,4), (11,2), (41,4) and (41,2). The second figure shows another visualization, by overlaying the filtered signal on top of the raw data. In this case, the input parameters window size and order were (201,2).

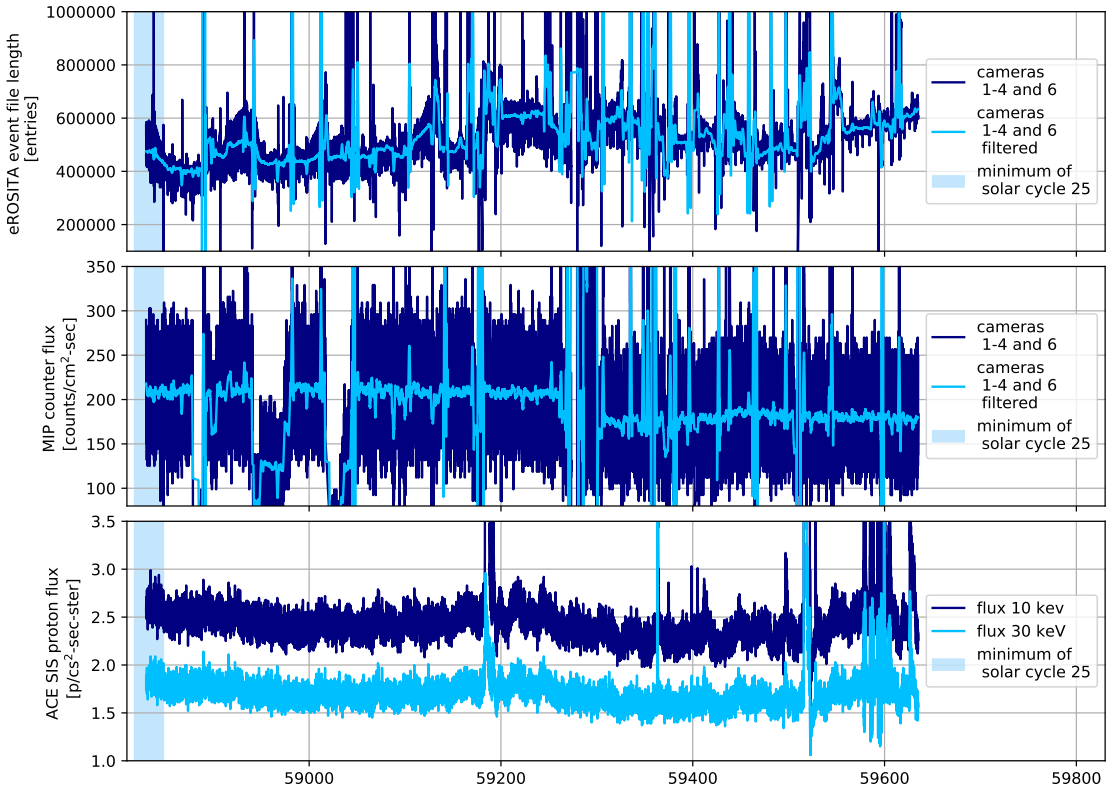

Figure 11: Comparison of the data sets in linear scale to investigate the constant background, whose major contribution are the galactic cosmic rays. As the beginning of the time interval coincides with the minimum of the solar cycle 25, we expect a gradual decrease of the inversely related galactic cosmic rays. This holds true, however, additional modulations appear due to the interaction between solar and galactic cosmic rays.

4.4. The solar event around MJD 59180

After studying the aspect concerning the galactic cosmic rays, we now want to move on the the contribution by solar cosmic rays. Therefore, we move on to inspecting the short-term behaviour of the MIP counter flux. From the overview over a timeline of approximately two years as shown in the figures up until now, we cannot really make out or analyze discrete solar events. Moreover, since more than only the solar wind contribute to the MIP readout of the raw eROSITA data, the solar activity is not discernible at first impression. However, by following the ACE data by eye, we can easily see at what times the sun was active and experienced solar flares. Therefore, by following the findings of the ACE data set, we can focus our view of the MIP data on the indicated time ranges that show solar outbursts. In this project, we chose to look at the intervals around MJDs 59180 and 59515. These will be discussed separately in the following two sections.

In Fig. 12, the overall comparison limited to the time interval from MJD 59181 to 59198.5 is shown. For this illustration, we extracted event and MIP files with a time resolution of 12 sec. We can see a small correlation between the MIP and ACE flux regarding the second burst around MJD 59191, however the beginning increase of the solar flare around MJD 59183 cannot be observed in eROSITA data. We explain this by the low intensity of high-energy particles in this

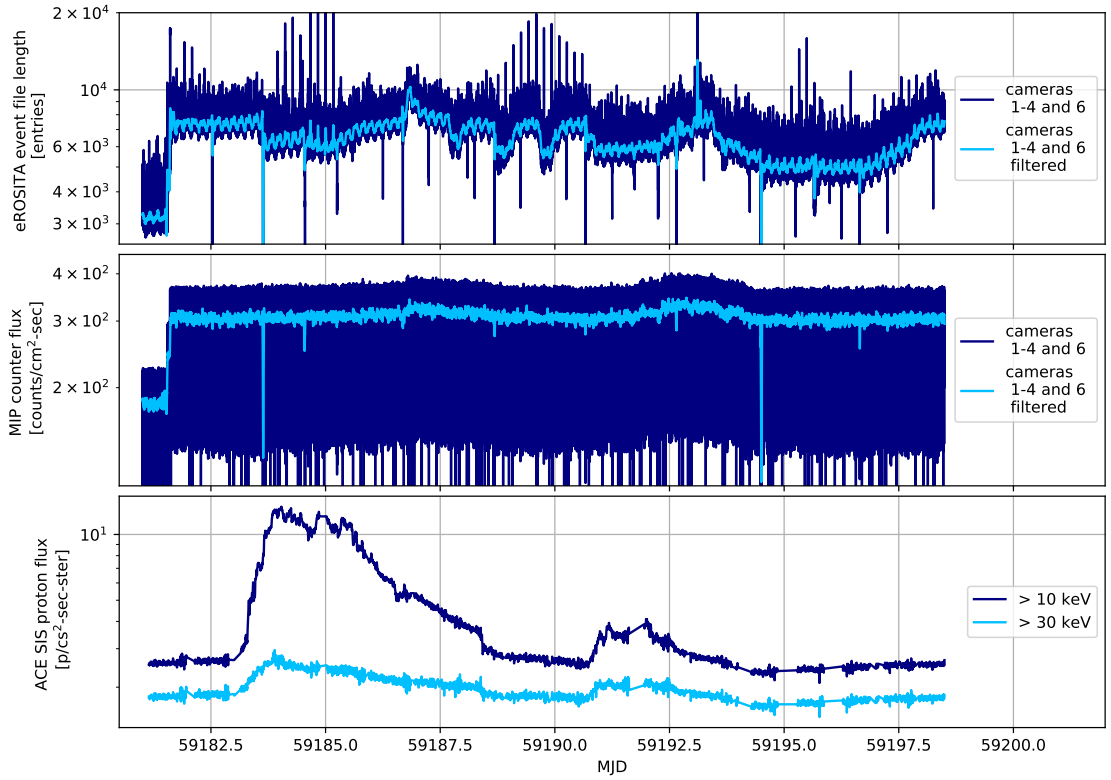

Figure 12: Extracted data for the solar event around November/December 2020. We can see almost no correlation between the ACE and MIP flux. This is explained due to the comparably low flux intensity of high energy particles in the burst, as seen in the ACE flux at the bottom.

event (see in the ACE flux $> 30\,\text{keV}$), which form the major contribution to MIPs. This is further investigated in the next section, Section 4.5, where we discuss another solar flare measured in our considered time interval.

Additionally, we can detect the effect of the high intensity optical light penetrating through the filter and contributing to the photon count in the event file length, as we previously discussed in Section 2.1.2. In the figure, one can clearly distinguish the angle dependent oscillation with a period of one rotation of eROSITA of 4 hrs per eROday.

4.5. The solar event around MJD 59515

In this section, we look in closer detail at the solar flare around MJD 59515. Like in the previous section, we extracted event and MIP files with a time resolution of 12 sec. Comparing the solar event to the one around MJD 59180, we note a significant increase in flux intensity in the ACE data in both energy ranges.

In this case, we can easily recognize a correlation between ACE and eROSITA data, as the starting increase is clearly visible in all three data sets. This was not the case before, which supports our assumption about the significance of high-energy protons in the flux. Therefore, from analyzing both figures on solar events, we can conclude that high energy particles contribute more strongly to

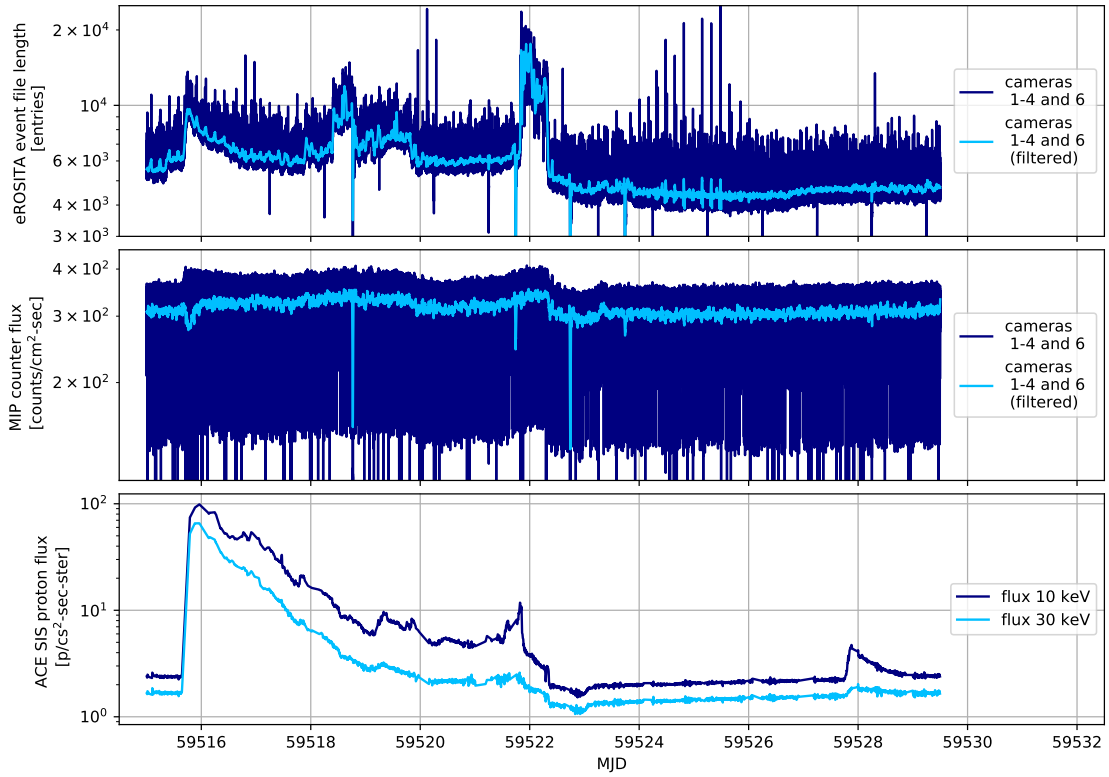

Figure 13: Extracted data for the solar event around October 2021. Here, all three data sets show a visible increase at the beginning of the flare. The resemblance of ACE and eROSITA data continues throughout the whole solar event. This confirms our claim about high energy particles being the major contributor to the MIP flux in eROSITA.

the MIP counter than particles with lower energy. This can additionally be confirmed with the small follow-up peak at around MJD 59528, which is only represented in the low energy contribution in ACE. Just like in Fig. 12, no increase is visible in eROSITA MIP flux data. With these results, we conclude that low energy particles are efficiently blocked by the eROSITA shielding, whereas high energy particles can penetrate more easily and arrive at the cameras.
Moreover, we can observe here, how accurate the rejection algorithm of eROSITA works. As we see the solar flare both in the MIP and the event data, we have proven the necessity to always also perform a subsequent background analysis on ground. This confirms what we already stated in Section 2.1.3.

4.6. Influence of the Milky Way

Because eROSITA is always rotating in a continuous manner, we expect the rate of MIPs to be varying as well in the rotation period of 4 hrs. To measure this influence of the galactic plane, we created a modified data file, where we eliminated all data points with a galactic latitude between $-20°$ and $20°$. When presenting the resulting content of the modified file in a histogram, see Fig. 14, we observe that the overall number of MIPs is reduced as expected, however the shift to a lower flux is not that significant. In the extracted data, we obtain a mean value of

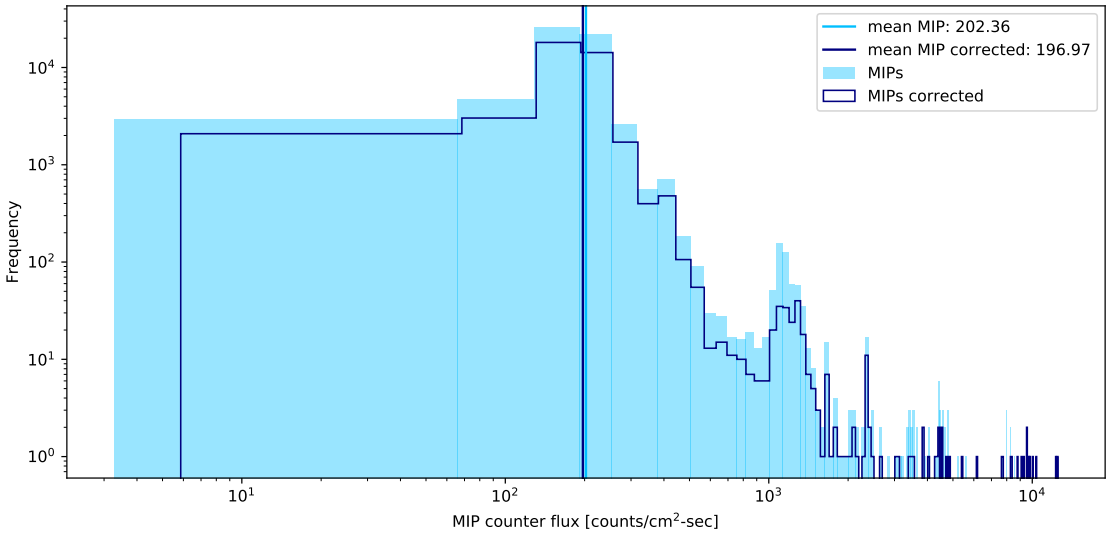

Figure 14: Histogram of the MIP counter flux to consider the influence of the Milky Way on the recorded MIP particles. We show the MIP counter flux before (light blue) and after (dark blue) the rejection of recorded values with an attitude between -20° and 20°. By comparing the two means, we see no significant reduction of high particle fluxes.

approximately $202.36\,\text{counts}\cdot\text{cm}^{-2}\cdot\text{sec}^{-1}$, which reduces slightly to $196.97\,\text{counts}\cdot\text{cm}^{-2}\cdot\text{sec}^{-1}$ after the excluding procedure. Therefore, the galactic plane seems to have no significant influence on the MIP count.

To further investigate this result, we depict a histogram of the recorded angles, according to which we excluded MIP values of Milky Way latitude in the modified file. Assuming a continuous rotation of eROSITA, we expect these values to be equally distributed over the whole angle range from -90° and 90°. The result is shown in the top of Fig. 15, not agreeing with our expectation. Other than an equal distribution of orientation angles, we observe a favoring of certain values, e.g., 0°. The angles appearing more often seem to follow a modulating 15°-long pattern. We assume this arises due to an influence of the chosen time resolution of 20 min. The mean of the attitude angle in one time unit is expected to be similar at each eROday. For $20\,\text{min} = 1200\,\text{sec}$ intervals, we would predict an angle resolution ρ of approximately

$$\rho = 360^\circ \cdot \frac{1200\,\text{sec}}{14400\,\text{sec}} = 30^\circ\,. \tag{2}$$

Therefore, we present the mean attitudes in 20 min resolution, resulting in six time intervals per eROday in the bottom of Fig. 15 for comparison. Nevertheless, this is only an assumption and to confirm it or find any other explanation, further investigation on this section is imperatively necessary.

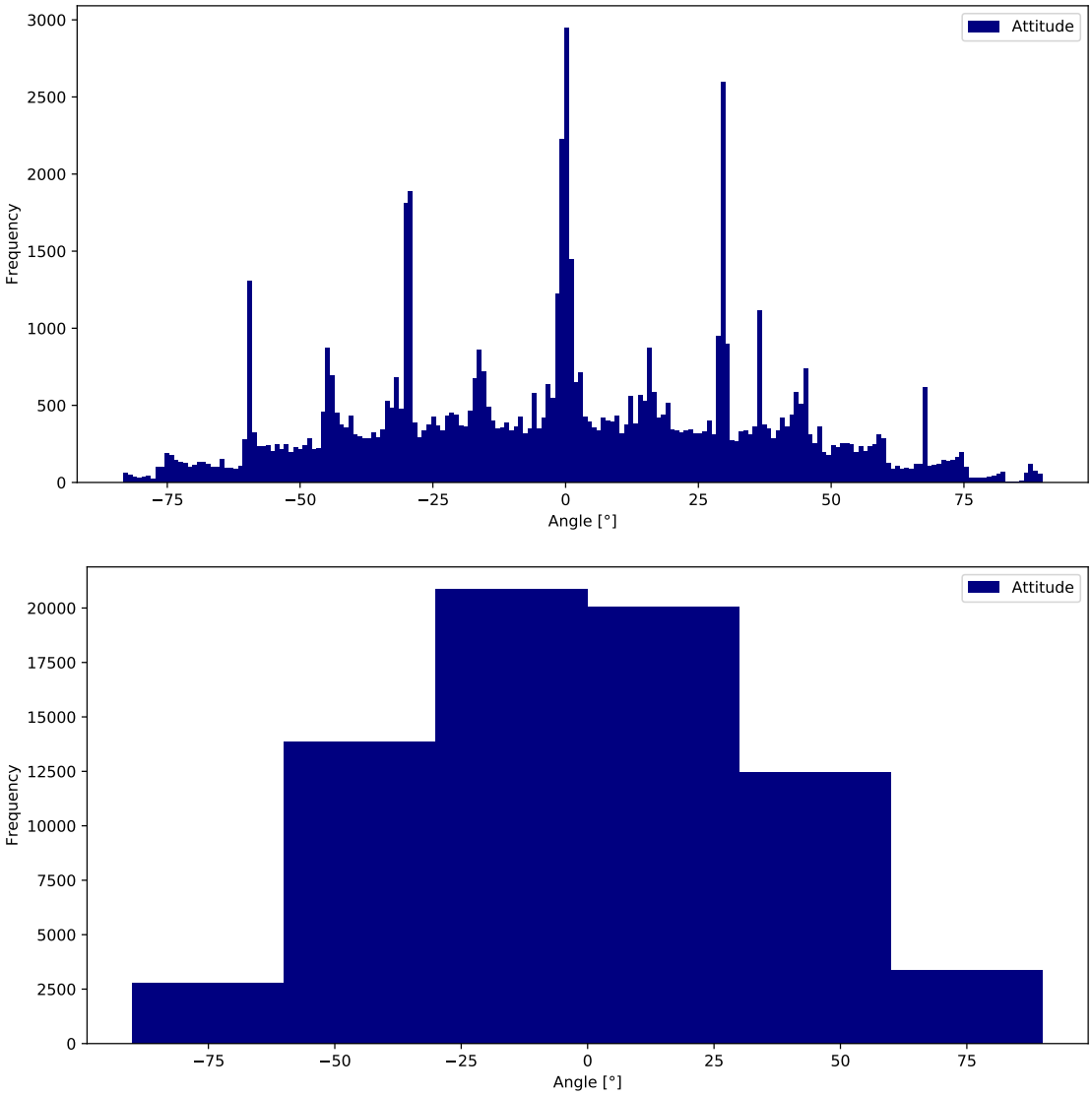

Figure 15: Histograms of the angle distribution. We show the attitude angles extracted for the whole time span in 200 (top) and 12 (bottom) bins. In the top figure, not according to our assumption, certain angle orientations appear more frequently than others, apparently in a 15° step-like fashion. However, when considering the time resolution of 20 min, which corresponds to 30°, a smooth distribution emerges.

4.7. Cross correlation

Due to the unequal distances of eROSITA and ACE to the sun, we expect a time difference of incoming solar cosmic particles between the two data sets. As explained before, ACE is located around the L_1 Lagrangian point, whereas eROSITA moves in a stable orbit around the L_2 Lagrangian point. The locations can be compared in Fig. 2a.

This time lag can be investigated by cross correlating the data sets. However, before we make use of our extracted data, we can easily calculate what delay is expected: Both Lagrangian points L_1 and L_2 are at a distance of $d = 0.01\,\mathrm{AU} = 1.5 \cdot 10^6\,\mathrm{km}$ from the earth. To approximate the MIP

velocity, we will use a typical value for the fast solar wind of around $v_{\text{wind}} \approx 750\,\text{km/sec}$ (Geiss, Gloeckler, and Steiger, 1995). We can therefore expect a time lag t_{lag} in the range of:

$$t_{\text{lag}} = \frac{2 \cdot d}{v_{\text{wind}}} \approx \frac{2 \cdot 1.5 \cdot 10^6\,\text{km}}{750\,\frac{\text{km}}{\text{sec}}} = 2000\,\text{sec}\,. \tag{3}$$

Now, we will compare this to the value resulting from the detector data. Using a cross correlation, we will extract a time lag that is experienced between the two detectors. In Fig. 16, said cross correlation is plotted. In the top plot, we consider the whole extracted interval, which results in a time lag of $-1200 \pm 1200\,\text{sec}$. The considered uncertainty originates simply in the time resolution of the extracted data. Therefore, we cannot observe a significant time lag here. This is expected, as the contribution of galactic cosmic rays should not present said time lag and the influence of solar events gets lost in the whole data.
However, when considering only the time around the solar event at approximately MJD 59515, a non-negligible time lag arises. This is shown in the bottom of Fig. 16. In the limited time interval, the cross correlation calculates a time lag of $1500 \pm 300\,\text{sec}$. Again, the uncertainty represents the binning of the extraction process, resulting in the time resolution. Using Equation 3, we can now also go backwards and calculate an updated velocity for the MIPs arriving at both detectors. We get

$$v_{\text{MIP}} = \frac{2 \cdot d}{t_{\text{lag}}} = \frac{2 \cdot 1.5 \cdot 10^6\,\text{km}}{1500 \pm 300\,\text{sec}} = 1000^{+250}_{-167}\,\frac{\text{km}}{\text{sec}}\,. \tag{4}$$

This velocity result is now larger than the typical value for the solar wind, however still in the same magnitude. We conclude, that the high energy particles that arrive at the cameras of the eROSITA detector are typically faster than the average of the fast solar wind. This is understandable, as we presume the low energy particles contributing to the average of the fast solar wind move with a lower velocity and are stopped by the shielding more easily.

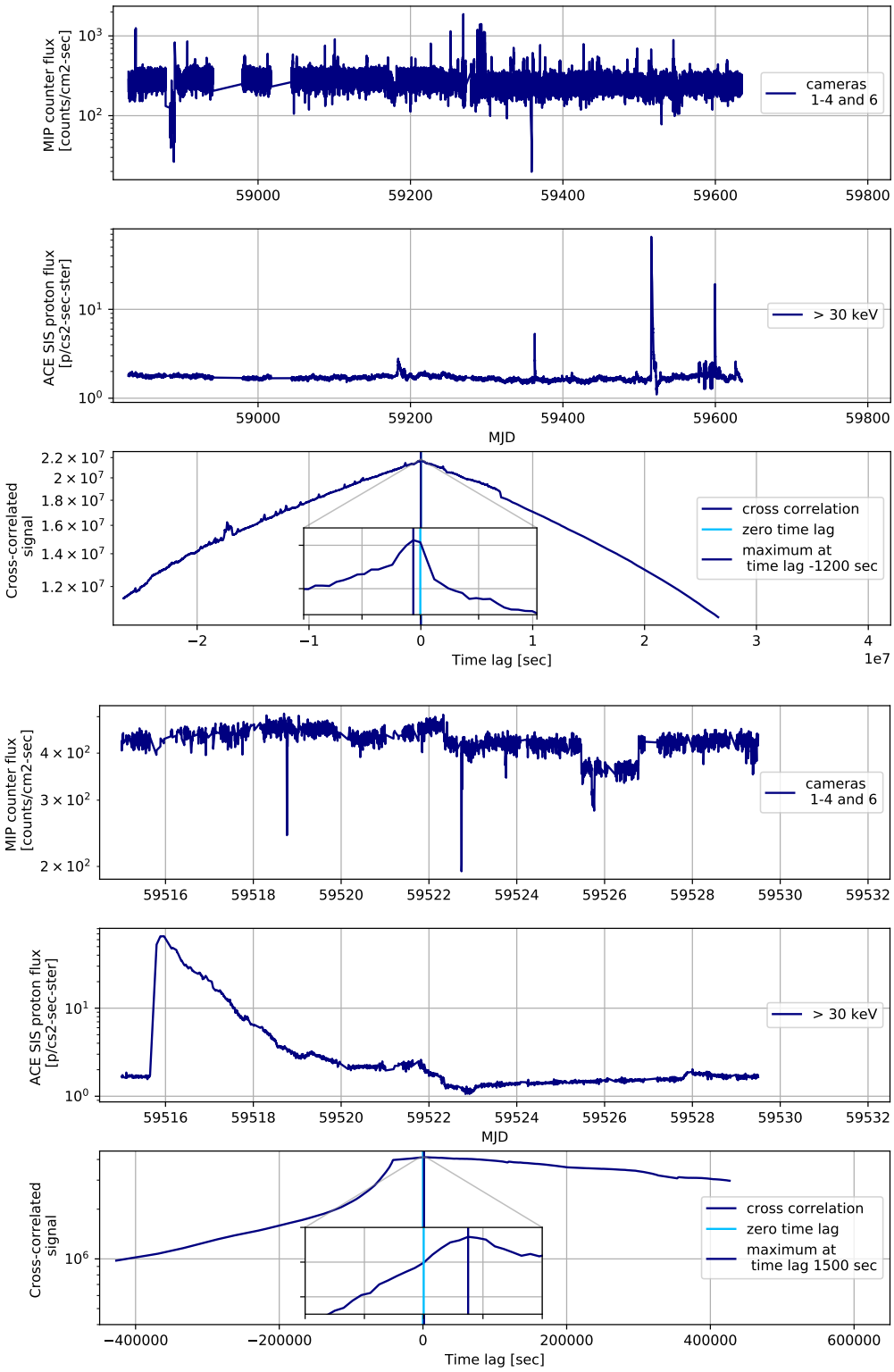

Figure 16: Cross correlations of the MIP counter flux with the high energy component of the ACE proton flux. Top: Cross correlation for the whole extracted time interval. As expected, we observe a negligible time lag $t_{\text{lag}} = 1200 \pm 1200\,\text{sec}$. Bottom: Cross correlation for the solar event in October 2021. Here, we obtain a time lag of $t_{\text{lag}} = 1500 \pm 300\,\text{sec}$.

5. Conclusion and Outlook

In this report we presented a comparison of MIP counter background data from eROSITA with space weather numbers from the sun-monitoring satellite ACE.
We started by summarizing the nature of cosmic rays and noted some differences between solar and galactic rays. Then, we presented the X-ray detector eROSITA and discussed possible background sources, specifically the one caused by cosmic rays. There, we also gave insight on how background is handled by explaining its rejection algorithm. After that, the sun-monitoring satellite ACE was briefly introduced.
We continued by documenting the data-extraction process developed for MIP data from the raw archive of eROSITA and briefly remarked how the comparative ACE data was obtained. Following this, we began analyzing the data and comparing it to measurements from the SIS detector on the ACE satellite. Starting with an overall comparison, we showed the data and how we modified it to simplify the analysis. Particularly, we visualized how data is smoothed by the application of varying Savitzky-Golay filters.
We investigated the contribution of galactic cosmic rays by considering the long-term evolution of the continuous MIP flux and observed that it is declining throughout the measurement time interval due to the minimum in solar activity at the starting time. Furthermore, we looked at two short-lived solar events, around MJDs 59180 and 59515, in more detail. The first one showed no definite visible change in the MIP counter data compared to the rising flux of protons measured by ACE at the start of the flare, however later throughout the event, some similarities could be recognized. In the second case, we could identify a sudden increase in eROSITA event and MIP numbers at the time of the sun-event detected in ACE, followed by a correlating shape in the decreasing part. In our short-term analysis, we showed their stronger agreement with the high energy proton flux on ACE. Consequently, we concluded that the shielding on eROSITA is more effective for low-energy particles than for ones with a higher energy, which therefore are detected by the cameras more frequently.
Moreover, we analyzed the influence by the galactic plane on our data by excluding measurements taken around the galactic equator. Here, we discovered that said influence appears to be negligible since no significant reduction in high measurement numbers was visible. However, we noted that this issue needs to be investigated in further detail. Lastly, we performed a cross correlation between the MIP and the ACE data both on the overall time interval and on the close-up of the solar event around MJD 59515. In the latter, we obtained a non-negligible time lag between the data sets and calculated a velocity estimate of the MIPs arriving at the cameras.
With these results, we gained insight on the space weather environment at the L_2 Lagrange point and the effectiveness of eROSITA's rejection algorithm. Moreover, by developing a process to extract MIP data from eROSITA, a detector primarily focusing on X-ray detection, we opened a pathway of using the detector for multifunctional detection and establishing a comprehensive method to oversee the effect of high-energy particles on outer-space measurements. Finally, the extraction of MIP flux data at the L_2 Lagrange point will prove to be helpful to monitor the cosmic wind at this highly important location for astrophysical projects.

However, the issues in this project are yet to be completely resolved and we recommend further investigation to understand the issue of space weather affecting outer-space detectors in order to apply our findings on future research. Directly concerning the extracted data of eROSITA, we propose the following options to continue:
As addressed in Section 4.3, the considered time interval is rather short when looking at the baseline flux contribution of galactic cosmic rays to the MIP counter flux. Therefore, we propose to extract a larger time period, so that the long-term behaviour could be studied in more detail. With this results, the statements made in this chapter about the decrease of flux by galactic cosmic rays would gain more weight. For instance, one could extract all data after the all-sky-surveys are completed. The total survey duration of four years, as noted in Section 2, would give a substantial overview, with which the expected decrease in galactic cosmic ray flux should be perfectly discernible.
Additionally, by extending this project for a long time, one could provide a long-term analysis of MIP data to visualize the increasing sun activity over the next years. This could be helpful to analyze, so that the relevance of background data initiated by cosmic rays is realized for future survey analyses.
Moreover, the ACE data, see for example in Fig. 11, shows small oscillations. As this was also discovered in Gaia background flux contributions (Kirsch, 2018), one could attempt to visualize this in eROSITA data as well. This could be achieved by e.g., rebinning the data over several eROdays by changing the time resolution in the extraction program.
As mentioned briefly above, further examination of the angle distribution and the influence by the galactic plane is required. The current results cannot be explained properly and many reasons could be responsible for that. We currently assume that the MIP selection and angle extraction processes are influenced by the chosen time resolution of 20 min, which is motivated by the unequal angle distribution depicted in Fig, 14. To approach this problem from a different perspective, it could prove to be helpful to overlay the MIP counter flux data of different eROdays on top of each other to compare the intensity variation throughout one eROday.
To get more accurate information on the time lag discussed in Section 4.7, one could acquire data from ACE providing information on X-ray flashes. Due to their velocity being the speed of light, X-ray flashes would help to derive a more precise arrival time difference between them and high-energy particles only on ACE. Consequently, we could extract more exact values for the MIP particle velocity. The same could be achieved as well by acquiring more extensive data from ACE with a higher time resolution than the 5 min that were used here, which would reduce our uncertainty in the time lag result.
Moreover, the methods of extraction and analysis in this project could be further developed to implement simultaneous read out of cosmic ray and X-ray fluxes in future detector electronics. This would improve the detection efficiency of a single spacecraft and also simplify on-ground analysis of measured data afterwards, since the cosmic ray flux and the damage on the detector can be monitored and accessed directly. Also, data gained from eROSITA MIP data could provide useful knowledge for preventive methods to save detector material from degrading and prolonging off-ground detector lifetimes.
In the future, this research project can be continued by additionally comparing the extracted data

from eROSITA to equivalent data withdrawn from GAIA (Garcia et al., 2018). As extraction pipelines already exist and could be provided (Kirsch, 2018), this also presents a time-efficient next step to analyze the cosmic ray environment at the L_2 Lagrange point more extensively (Freyberg et al., 2020). Then, one could analyze two data sets from different missions that measured there and compare the influence by cosmic rays on the detectors with respect to their orbits. This could prove to be extremely helpful when preparing future missions planned at that location.

References

Adams, L. (1985), *Microelectronics Journal* **16**, 17

Anchordoqui, L. A. (2019), *Physics Reports* **801**, 1

Blasi, P. (2013), *The Astronomy and Astrophysics Review* **21**, 70

Crowley, C. et al. (2016), *Astronomy and Astrophysics* **595**, A6

Freyberg, M. et al. (2020), in: *Space Telescopes and Instrumentation 2020: Ultraviolet to Gamma Ray*, ed. by Herder, J.-W. A. den, Nikzad, S., & Nakazawa, K., vol. 11444, Society of Photo-Optical Instrumentation Engineers (SPIE) Conference Series, International Society for Optics and Photonics, SPIE, 114441O

Friedrich, P. et al. (2008), in: *Space Telescopes and Instrumentation 2008: Ultraviolet to Gamma Ray*, ed. by Turner, M. J. L. & Flanagan, K. A., vol. 7011, Society of Photo-Optical Instrumentation Engineers (SPIE) Conference Series, International Society for Optics and Photonics, SPIE, 70112T

Garcia, L. et al. (2018), in: *High Energy, Optical, and Infrared Detectors for Astronomy VIII*, ed. by Holland, A. D. & Beletic, J., vol. 10709, Society of Photo-Optical Instrumentation Engineers (SPIE) Conference Series, International Society for Optics and Photonics, SPIE, 1070919

Geiss, J., Gloeckler, G., & Steiger, R. von (1995), *Space Science Reviews* **72**, 49

Geryl, P. P. A. & Alvestad, J. (2020), *Astrophysics and Space Science* **365**, 113

Hathaway, D. H. (2015), *Living Reviews in Solar Physics* **12**, 4

Hess, V. F. (1912), *Physikalische Zeitschrift* **13**, 1084

Horne, R. B. et al. (2013), *Space Weather* **11**, 169

Hoyt, D. V. & Schatten, K. H. (1998), *Solar physics* **179**, 189

Iskra, K. et al. (2019), *Solar Physics* **294**, 115

Kirsch, C. (2018), *The Cosmic Ray Background at L2 as Seen in Gaia Observations*, MA thesis, Friedrich-Alexander-Universität Erlangen-Nürnberg

Max Planck Institute for extraterrestrial Physics (2020), *Our deepest view of the X-ray sky*, URL: https://www.mpe.mpg.de/7461761/news20200619 (visited on 2022)

Meidinger, N. et al. (2014), in: *Space Telescopes and Instrumentation 2014: Ultraviolet to Gamma Ray*, ed. by Takahashi, T., Herder, J.-W. A. den, & Bautz, M., vol. 9144, Society of Photo-Optical Instrumentation Engineers (SPIE) Conference Series, International Society for Optics and Photonics, SPIE, 91441W

Merloni, A. et al. (2012), *arXiv e-prints*, arXiv:1209.3114

NASA/WMAP Science Team (2018), *Our deepest view of the X-ray sky*, URL: https://solarsystem.nasa.gov/resources/754/what-is-a-lagrange-point/ (visited on 2023)

Padovani, P. et al. (2017), *The Astronomy and Astrophysics Review* **25**

Pavlinsky, M. et al. (2018), in: *Space Telescopes and Instrumentation 2018: Ultraviolet to Gamma Ray*, ed. by Herder, J.-W. A. den, Nikzad, S., & Nakazawa, K., vol. 10699, Society of Photo-Optical Instrumentation Engineers (SPIE) Conference Series, International Society for Optics and Photonics, SPIE, 106991Y

Perinati, E. et al. (2012), *Experimental Astronomy* **33**, 39

Pillepich, A., Porciani, C., & Reiprich, T. H. (2012), *Monthly Notices of the Royal Astronomical Society* **422**, 44

Predehl, P. et al. (2021), *Astronomy and Astrophysics* **647**, A1

Reames, D. V. (1999), *Space Science Reviews* **90**, 413

Schwenn, R. (2006), *Living Reviews in Solar Physics* **3**, 2

SILSO, R. O. o. B. (2014), *Sunspot Index and Long-term Solar Observations (SILSO)*, URL: http://sidc.oma.be/silso/

Stone, E. C. et al. (1998a), *Space Science Reviews* **86**, 1

Stone, E. C. et al. (1998b), *Space Science Reviews* **86**, 357

Sullivan, J. D. (1971), *Nuclear Instruments and Methods* **95**, 5

Tanabashi, M. et al. (2018), *Physical Review D* **98**, 030001

Tenzer, C. et al. (2010), in: *High Energy, Optical, and Infrared Detectors for Astronomy IV*, ed. by Holland, A. D. & Dorn, D. A., vol. 7742, Society of Photo-Optical Instrumentation Engineers (SPIE) Conference Series, International Society for Optics and Photonics, SPIE, 77420Y

Tomassetti, N. et al. (2017), *The Astrophysical Journal Letters* **849**, L32

Truemper, J. (1982), *Advances in Space Research* **2**, 241

Voges, W. et al. (1999), *Astronomy and Astrophysics* **349**, 389

Wolf, R. (1861), *Monthly Notices of the Royal Astronomical Society* **21**, 77

– (1877), *Astronomische Mitteilungen der Eidgenössischen Sternwarte Zurich* **5**, 29

Zwickl, R. D. et al. (1998), *Space Science Reviews* **86**, 633

A. Appendix

A.1. Example of extraction code

Here, we show an example of our extraction code for the MIP counter. The code is explained in Section 3.1.

```
#import all relevant packages
import numpy as np
import glob
from astropy.io import fits
from astropy.table import Table
from astropy.time import Time


#functions to switch between erodays and mjd:

ero_one_utc = ['1999-12-31T21:00:00'] #eroday one is 2000-01-01
    in moscow time and utc to moscow are +3hrs
time_ero_one = Time(ero_one_utc, format = 'isot')
ero_one_mjd = time_ero_one.mjd #transform eroday one into mjd
eroday_sec = 14400 #one eroday in seconds

def eRO_to_MJD(eRO_day):
    days = (eRO_day-1)/6     #days since eroday one
    return ero_one_mjd + days

def MJD_to_eRO(MJD):
    return ((MJD-ero_one_mjd)*6+1)

#input parameters: time resolution and time interval
#time resolution
time_div = 12 #this will resolve to 1200 sec (calculate the time
    resolution by dividing 4h by this number)
#time interval
tstart = int(MJD_to_eRO(58700))
tstop = int(MJD_to_eRO(59380))

#create empty file
mip_table = Table([[],[],[],[],[],[],[],[],[]],names = ('eRO_day
    ','eRO_day_res', 'event-ctr_cam1','event-ctr_cam2','event-
    ctr_cam3','event-ctr_cam4','event-ctr_cam5','event-ctr_cam6',
```

```
    'event-ctr_cam7'))

#iterate over time interval (in erodays)
for i in range(tstart,tstop):

    #start with time entries, first column:
    eRO_day = int(i)
    #get first 3 and remaining 2 digits to find the files in the
        folder directory
    eRO_day_front = int(np.floor(eRO_day/100))
    eRO_day_back = eRO_day - eRO_day_front*100
    #get resoluted time range in erodays
    eRO_day_res = np.arange(i,i+1,1/(time_div))

    #create one list to save all camera entries of one entry (
       will be one row in the mip_table)
    mip_list = [0,0,0,0,0,0,0,0,0]

    #create variable 'partial' to move within one eroday, move
       through variable with for-loop
    partial = 0
    for j in eRO_day_res:

        #insert time into list
        mip_list[0]= eRO_day
        mip_list[1] = j

        #iterate over all cameras
        for k in range(1,8):
            #get filename with mip column, either mips are
               counted in HKA8 (trigger and sum in HKA9
               separately) or in HKAA combined, depending on
               amount
            try:
                basedir = glob.glob("/data/X-ray/eROSITA/
                   rawArchive/fits/{}/{}/eROSITA/H_SciHKA8_{}_{}
                   _00*_P003.fits".format(eRO_day_front,"%02d" %
                    eRO_day_back,k,eRO_day))

                #open file
                rawdata = fits.open(basedir[0])
```

```
            mip_events = Table(rawdata[1].data)
            rawdata.close()

            #get time range in erodays
            eRO_time_min = (eRO_day-1) *eroday_sec
            eRO_time_res_min = eRO_time_min + partial * (
               eroday_sec/time_div)
            eRO_time_res_max = eRO_time_min + (partial+1)*(
               eroday_sec/time_div)

            #get table limited to chosen time resolution
            mip_ev_min = mip_events[mip_events['RecordTime'
               ]>eRO_time_res_min]
            mip_ev_res = mip_ev_min[mip_ev_min['RecordTime'
               ]<eRO_time_res_max]

            #count the mip counter

            #start with first entry
            mip_1 = 0 - mip_ev_res["MIP-pixel"][0] #subtract
                first entry (column is summed up -> first
               entry is counted mip number before the
               interval)

            #iterate over mip column
            for x in range(len(mip_ev_res["MIP-pixel"])-1):

                #if we go over counting limit add 2**16
                if mip_ev_res["MIP-pixel"][x+1]<mip_ev_res["
                   MIP-pixel"][x]:
                    mip_1 +=65535

            #add last entry
            mip_1 += mip_ev_res["MIP-pixel"][-1]

            #insert counted mip value in list for table row
            mip_list[k+1] = mip_1

        #try other housekeeping file, do everything like in
           case above, only difference: capital P in column
           name 'MIP-Pixel'
```

```
            except IndexError:
                try:
                    basedir = glob.glob("/data/X-ray/eROSITA/
                        rawArchive/fits/{}/{}/eROSITA/H_SciHKAA_
                        {}_{}_00*_P003.fits".format(eRO_day_front
                        ,"%02d" % eRO_day_back,k,eRO_day))

                    rawdata = fits.open(basedir[0])
                    mip_events = Table(rawdata[1].data)
                    rawdata.close()

                    eRO_time_min = (eRO_day-1) *eroday_sec
                    eRO_time_res_min = eRO_time_min + partial *
                        (eroday_sec/time_div)
                    eRO_time_res_max = eRO_time_min + (partial
                        +1)*(eroday_sec/time_div)

                    mip_ev_min = mip_events[mip_events['
                        RecordTime']>eRO_time_res_min]
                    mip_ev_res = mip_ev_min[mip_ev_min['
                        RecordTime']<eRO_time_res_max]

                    mip = 0 - mip_ev_res["MIP-Pixel"][0]
                    for z in range(len(mip_ev_res["MIP-Pixel"])-
                        1):
                         if mip_ev_res["MIP-Pixel"][z+1]<
                            mip_ev_res["MIP-Pixel"][z]:
                             mip +=65535
                    mip += mip_ev_res["MIP-Pixel"][-1]

                    mip_list[k+1] = mip # * 1/measure_ratio

                #if nothing is saved (e.g., at the beginning)
                except IndexError:
                    print('nothing␣found') #show where no file
                        was found, if suspicious, we can follow
                        up


        #move one up in partial counter for next time interval
        partial = partial + 1
```

```
            print(mip_list) #show result during readout

            #add extracted row to table
            mip_table.add_row(mip_list)

#save table as fits with annotation of time resolution and
    interval
mip_table.write("mip_number_{}_lengths_eROSITA_period{}to{}.fits
    ".format(int(eroday_sec/time_div),tstart,tstop), format = '
    fits')
```